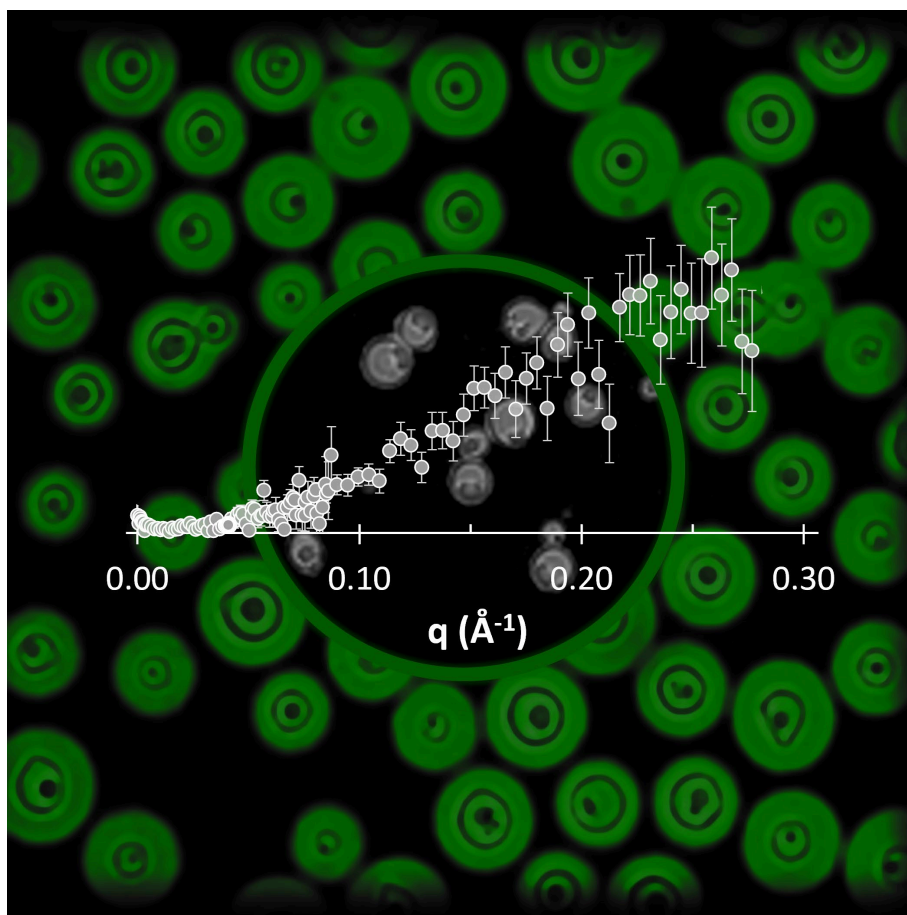


Neutron Scattering Analysis of the *Cryptococcus neoformans* Polysaccharide Reveals Solution Rigidity and Repeating Fractal-like Structural Patterns

Ziwei Wang¹, Susana C. M. Teixeira^{2,3, *}, Camilla Strother¹, Anthony Bowen¹, Arturo Casadevall¹, and Radamés JB Cordero^{1, *}

¹Department of Molecular Microbiology and Immunology, Johns Hopkins Bloomberg School of Public Health, Baltimore, Maryland, 21205, USA. ²NIST Center of Neutron Research, National Institute of Standards and Technology, Gaithersburg, Maryland, 20899, USA. ³Department of Chemical and Biomolecular Engineering, University of Delaware, Newark, Delaware, 19716, USA. *Corresponding authors.



Artistic green colored rendering of a microscopy image of *Cryptococcus neoformans* H99 cells, where the inner circle shows the cells after gamma irradiation. A Kratky plot from Small Angle Neutron Scattering data is superposed, capturing a core finding of the local *Cryptococcus* polysaccharide structure.

1 **ABSTRACT:** *Cryptococcus neoformans* is a fungal pathogen that can cause life-threatening brain
2 infections in immunocompromised individuals. Unlike other fungal pathogens, it possesses a
3 protective polysaccharide capsule crucial for its virulence. During infections, *Cryptococcus* cells
4 release copious amounts of extracellular polysaccharides (exo-PS) that interfere with host immune
5 responses. Both exo-PS and capsular-PS are pivotal in *Cryptococcus* infections and represent key
6 targets for disease diagnosis and vaccine development strategies. However, understanding their
7 structure is complicated by their polydispersity, complexity, sensitivity to sample isolation and
8 processing, and scarcity of methods capable of isolating and analyzing them while preserving their
9 native structure. In this study, we employ small-angle neutron scattering (SANS) and ultra-small
10 angle neutron scattering (USANS) for the first time to investigate both fungal cell suspensions and
11 extracellular polysaccharides in solution. Our data suggests that exo-PS in solution exhibits
12 collapsed chain-like behavior and demonstrates mass fractal properties that indicate a relatively
13 condensed pore structure in aqueous environments. This observation is also supported by scanning
14 electron microscopy (SEM). The local structure of the polysaccharide is characterized as a rigid
15 rod, with a length-scale corresponding to 3 to 4 repeating units. This research not only unveils
16 insights into exo-PS and capsular-PS structures but also demonstrates the potential of USANS for
17 studying changes in cell dimensions and of the promise of contrast variation in future neutron
18 scattering studies.

1 INTRODUCTION

2 Cryptococcal meningitis is a deadly fungal infection caused by *Cryptococcus neoformans*, one
3 of the leading causes of death in HIV/AIDS patients in sub-Saharan Africa^{1,2}. Within brain tissues,
4 the fungus secretes copious amounts of polysaccharide (exo-PS) to the cerebrospinal fluid,
5 believed to cause elevated intracranial pressure and disruption of an effective immune response^{2,3}.
6 The fungal cell is encased by a thick capsule composed of polysaccharide (capsular-PS), which
7 protects from the host's immune defense mechanisms⁴. Both the exo-PS and capsular-PS are
8 mainly comprised of glucuronoxylomannan (GXM), which is formed by an α -1,3-linked mannan
9 backbone with β -1,2-linked glucuronic acid and β -1,2- or β -1,4-linked xylose as its branching
10 residues that contribute to serological diversity. GXM molecules are assembled from six structural
11 units (M1-6), referred to as triads, featuring a glucuronic acid residue every third mannose along
12 with varying xylose substitutions (Figure 1). Due to its high water-content (over 95% of total mass
13 and volume), the PS capsule is highly susceptible to the dehydration steps employed in high-
14 resolution microscopy or lyophilization, which disturbs the native structure^{5,6}.

15 *C. neoformans* exo-PS and capsular-PS are key virulence determinants and targets for the
16 immune system, vaccine design, and monoclonal antibody (mAb) treatments. Diagnosis of
17 *Cryptococcus* infection primarily relies on antibody-based methods^{7,8}. Although both exo-PS and
18 capsular-PS are predominantly composed of GXM, they exhibit distinct physicochemical
19 properties and mAb reactivity⁸. Despite their significance in disease and diagnosis, and the known
20 chemical composition of the GXM, the macro- and supramolecular assembly of the *Cryptococcal*
21 PS and the corresponding effects on epitope binding by antibodies remain largely unknown.
22 Studying the correlation between nanoscale structure and macroscopic properties of the PS, and

1 how both natural and experimental environments can trigger different assembly characteristics, is
2 crucial for the design of diagnostic assays and strategies for vaccine development.

3 The large and complex PS heteropolymers display physicochemical characteristics that vary
4 based on nutrient availability, chemical and physical environment, and cell age^{8,9}. Consequently,
5 experimental biases can be introduced by sample preparation protocols and the inherent limitations
6 of measurement techniques. Previous research has primarily focused on PS isolated from culture
7 supernatants using hexadecyltrimethylammonium bromide (CTAB) precipitation or filtration, and
8 capsular-PS extracted via dimethylsulfoxide (DMSO) extraction and ionizing radiation-induced
9 PS ablation, leading to nominally de-capsulated cells (residual capsular-PS may remain). A variety
10 of techniques, such as static (SLS) and dynamic light scattering (DLS), zeta potential
11 measurements, optical tweezers-based elastic modulus assessments, and solution viscosity
12 analyses, have been employed to investigate exo-PS and capsular-PS structure^{10,11}. SLS and DLS
13 analyses suggest that the polysaccharide molecules are branched, a characteristic that influences
14 immune reactivity and modulation¹²⁻¹⁵. Existing experimental data is consistent with capsular-PS
15 polymers in molar mass ranges of 1-7 MDa, radii of gyration (R_g) ranging from 150-500 nm,
16 hydrodynamic radii (R_h) ranging spanning 570-2000 nm, contingent on the specific experimental
17 method used^{10,13,16,17}. Encapsulated and nominally de-capsulated cells were previously
18 investigated by powder X-ray diffraction, where broad peaks in the range of 1.46 \AA^{-1} - 1.51 \AA^{-1} of
19 momentum transfer vector q , were attributed to a repeating structural motif arising from inter-
20 molecular interactions mediated by divalent metals, glucuronic acid residues, and/or possibly
21 gelled PS organization¹⁸. A detailed characterization of the relationship between the structures of
22 exo-PS and capsular-PS, and their corresponding functions at different stages of infection, requires
23 measurement capabilities that preserve PS conformation.

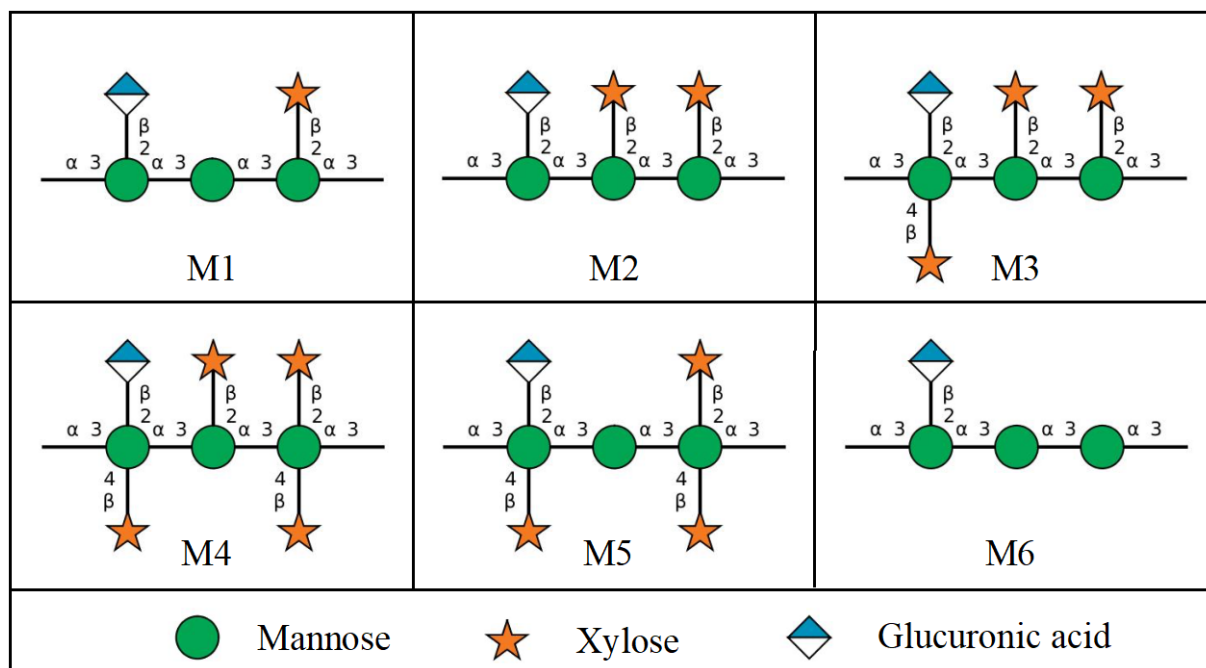
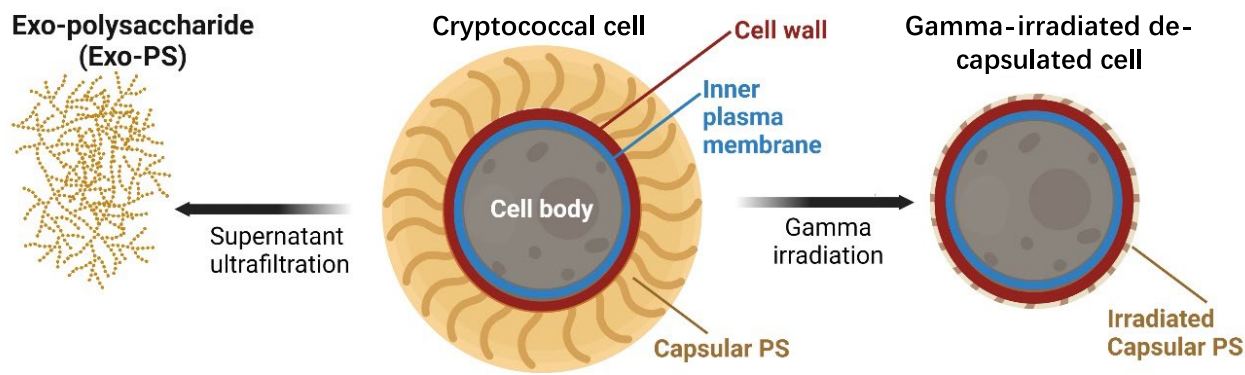


Figure 1. The six Glucuronoxylomannan (GXM) motifs that build up fungal exo-PS and capsular-PS. GXM is composed of a combination of six repeating units (M1-6), defined by a glucuronic acid (GlcA) residue every 3rd mannose with varying xylose substitutions. These 6 motifs of GXM in various combinations correlate to different serotype activities¹⁹. *C. neoformans* H99 serotype A has a dominant M2 motif in exo- and capsular-PS²⁰. Polysaccharide molecules can be heteropolymers composed of more than one triad¹⁷. Image created with DrawGlycan-SNFG²¹.

In this study, we used neutron scattering analyses, light microscopy and scanning electron microscopy to probe the structure of exo-PS, intact fungal cells, and gamma-irradiated nominally de-capsulated cells in solution (**Figure 2**). Neutron scattering accesses a broad range of structural features without causing radiation damage, enabling data collection on the same samples across small-angle (SANS) and ultra-small angle (USANS) neutron scattering regimes at various temperatures and concentrations. This approach has been previously used for studies of polysaccharides, such as arabinoxylans by Yu *et al.*²², and minimizes sample discrepancies, while the use of varying percentages of D₂O in buffers allows for contrast variation. Given the

1 considerable size of the cells (micrometers in diameter), the USANS regime is crucial, whereas
2 the analysis of intrachain structures is conducted within the SANS regime.

3



4

5 **Figure 2.** Schematic diagram of the samples investigated: exo-PS, cryptococcal cell, and gamma-
6 irradiated de-capsulated cell. Exo-PS refers to the secreted polysaccharide, while capsular-PS
7 refers to the highly hydrated polysaccharide surrounding the capsule of the intact cell. Gamma-
8 irradiated capsular-PS refers to the remaining polysaccharide thin capsule surrounding the
9 irradiated cells. Image created with BioRender.com.

10

11

12 MATERIALS AND METHODS

13 **Fungal Growth.** *Cryptococcus neoformans* Serotype A strain H99 was inoculated in 20 mL of
14 Sabouraud dextrose broth and grown with agitation (120 rpm) for 2 days at 30 °C. The cells were
15 pelleted by centrifuging for 10 minutes at 3000 rpm, and resuspended in minimal media (15 mM
16 dextrose, 10 mM MgSO₄, 29.3 mM KH₂PO₄, 13 mM glycine, and 3 μM thiamine-HCl, adjusted
17 to pH 5.5 using KOH; where ‘M’ represents the SI units mol/L). The washing process was repeated
18 three times, and the cells were finally resuspended in minimal media to a density of 1 × 10⁶
19 cells/mL. Subsequently, the cells were inoculated into a 1 L culture of minimal media and
20 incubated at 30 °C for 7 days. The cells were harvested via centrifugation at 4,000 rpm for 20
21 minutes. The supernatant was filtered using a 0.22 μm Millipore.

1 Capsular-PS was removed by exposing the whole cells to 40 minutes of gamma irradiation, using
2 the method demonstrated by Maxson *et al.*²³. The ionizing radiation was demonstrated to be
3 effective in removing the capsular-PS²⁴.

4
5 **Exo-PS Isolation.** The exo-PS was isolated from the cell-free supernatant as previously
6 described²⁵. The supernatant was sequentially filtered with an Amicon membrane filter (100 kDa
7 nominal molar mass cutoff) and the flow-through was then filtered using a 10 kDa membrane
8 filter. The exo-PS accumulated on the 10 kDa membrane surface as a clear gel and was collected
9 and dialyzed extensively against MilliQ-grade H₂O or D₂O (Cambridge Isotope Labs, 99.9% D).
10 The H₂O solutions provide scattering profiles at an additional contrast, while the samples prepared
11 in D₂O are expected to minimize the incoherent neutron scattering background contribution to the
12 measured intensity profiles. Following dialysis, the exo-PS concentration was determined using a
13 phenol sulfuric colorimetry assay²⁶. Sample solutions were centrifuged for 2 minutes at 10,000
14 rpm to remove any debris. This process resulted in 10mg/mL exo-PS samples with a hydrodynamic
15 radius R_h of 550-600 nm and relatively low polydispersity, quantified as 0.355 (**Figure S1**) by
16 DLS coupled with a 90Plus/BI-MAS Multi-Angle Particle Sizing analyzer (Brookhaven
17 Instruments Corp., NY, USA), as described by Frases *et al.*¹⁶. The prepared exo-PS was also
18 resuspended at 1 mg/mL and 5 mg/mL. Based on the equation derived by Vadillo *et al.*²⁷ ($c^* \approx$
19 $1.46/[\eta]$) and the intrinsic viscosity ($[\eta]$) of PS from strain H99 in minimal media determined by
20 Cordero *et al.*¹³, the overlap concentration c^* for exo-PS is estimated as 5 mg/mL.²⁸

21
22 **SANS and USANS Data Collection and Reduction.** Neutron scattering data were collected at
23 the National Institute of Standards and Technology (NIST) Center for Neutron Research (NCNR;

1 Gaithersburg, Maryland USA). All samples were degassed for 10 minutes before data collection.
2 SANS data were obtained from the 30-meter instruments NG7 and NGB, using a neutron
3 wavelength λ of 6 Å and a wavelength spread $\Delta\lambda/\lambda$ of 12.5 % for three sample-to-detector distances,
4 to measure scattered intensities over a range of momentum transfer defined as:

$$5 \quad q = \frac{4\pi \sin \theta}{\lambda} \quad (1)$$

6 where 2θ is the scattering angle measured. Focusing lenses were used for the longer wavelengths
7 (8.4 Å on NGB, and 8.09 Å on NG7) to extend the lower q range to 0.001 Å⁻¹ in the SANS
8 regime²⁹. Scattered neutrons were detected with a 64 cm × 64 cm 2D position-sensitive detector
9 with 128 pixels × 128 pixels at a resolution of 0.508 cm/pixel. SANS data measured for solutions
10 in H₂O at concentrations of exo-PS up to 10 mg/mL show a flat intensity profile in the q range
11 measured, indicative of insufficient contrast to provide a measurable signal above the strong
12 incoherent scattering background from the hydrogen atoms in the buffer (**Figure S2**). SANS
13 measurements were carried out on 1 mg/mL, 5 mg/mL, and 10 mg/mL of exo-PS solutions in D₂O
14 at three temperatures (22 °C, 30 °C, and 37 °C), controlled by a Peltier-driven sample changer,
15 with 30 minutes of pre-equilibration at the desired temperature before data collection. The
16 temperatures chosen include typical ambient experimental environments (22 °C), as well as the *C.*
17 *neoformans* optimal growth (30 °C), and physiological temperatures (37 °C). No significant
18 differences were observed between the SANS profiles of exo-PS solutions at the three measured
19 temperatures (data not shown): the profiles overlapped well, within experimental error. A
20 temperature of 30 °C was therefore chosen for data collection on the whole cells and gamma-
21 irradiated cells in the SANS and USANS regime, for consistency with the growth temperature of
22 the whole fungal cells.

1 Slit-smear USANS data were collected at the double-crystal diffractometer (Bonse-Hart) BT5
2 at the NCNR ($\lambda = 2.4 \text{ \AA}$, $\Delta\lambda/\lambda = 6\%$)³⁰, to cover a q range of 0.00003 \AA^{-1} to 0.003 \AA^{-1} . USANS
3 measurements were carried out on 10 mg/mL exo-PS in D₂O at 30 °C to probe the presence of
4 aggregates or finite size clusters or aggregates in the micrometer to hundreds of nanometers size
5 range. USANS data were also collected on D₂O and H₂O solutions of the whole fungal cells, and
6 gamma irradiated cells at the concentration of 1×10^8 cells/mL.

7 SANS and USANS data were reduced using the macro-routines developed for IGOR Pro at the
8 NCNR³¹. Raw counts were normalized to a common neutron monitor count and corrected for
9 empty cell counts, ambient background counts, and nonuniform detector response. The data
10 obtained from the samples were placed on an absolute scale by normalizing the scattered intensity
11 to the incident beam flux. Buffer-only reduced data were subtracted from SANS data on samples
12 containing exo-PS or capsular-PS.

13

14 **Neutron Scattering Data Fitting.** The SANS data for the exo-PS solutions in D₂O were fitted
15 using a modified empirical correlation length function that calculates scattering intensities as:

16
$$I(q) = \frac{A}{q^n} + \frac{C}{1 + (q\xi)^m} + B \quad (2)$$

17 where the first term describes Porod scattering from pore clusters (exponent n) and the second
18 term is a Lorentzian function describing scattering from the PS polymer chains (exponent m)³².
19 The second term characterizes the PS/solvent interactions, and the two multiplicative factors A and
20 C are, respectively, the Porod scale and the Lorentz scale. ξ is a correlation length for the PS chains,
21 and B is a q -independent incoherent neutron scattering intensity background contribution to $I(q)$.
22 The calculated intensities from the correlation length model were smeared to match the
23 instrumental pinhole smearing read from the reduced experimental data file. The exo-PS volume

1 fraction and the B parameter were kept fixed throughout the fits. The fitting parameters and
2 relevant information on the goodness-of-fit are available in the supporting information for the
3 interested reader (**Table S1**). It was assumed that the entanglement of overlapping PS chains did
4 not contribute significantly towards the SANS profiles..

5
6 **Light Microscopy.** To measure the cell and capsule dimensions, whole cells and gamma-
7 irradiated cells in D₂O and H₂O at 1×10^8 cells/mL were imaged with an Olympus AX70
8 microscope, using the QCapture Suite V2.46 software for Windows. *Cryptococcal* cells were
9 suspended in India Ink, which is excluded by the PS so that the capsule region will appear to be
10 bright/empty. Cell dimensions were measured with ImageJ in pixels, and then converted to μm
11 (152 pixels correspond to 50 μm for 40 \times magnification objective with 2 \times 2 binning). Statistical
12 analyses were performed using GraphPad Prism version 9.5.1 for Mac OS X, GraphPad Software,
13 Boston, Massachusetts USA. Unpaired statistical analyses t-tests were done for the cell diameters
14 and capsule thickness comparisons; the corresponding significance was stratified based on the
15 probability that the results occur by chance, quantified as a probability through a percentage p-
16 value, where 5% is equivalent to $p = 0.05$.

17
18 **Scanning Electron Microscopy.** SEM of encapsulated *C. neoformans* yeast cells was done as
19 previously described¹³. Briefly, the cells were fixed using a solution containing glutaraldehyde,
20 sodium Cacodylate, sucrose, and MgCl₂. After dehydration with ethanol, critical point drying was
21 performed using liquid carbon dioxide. The dried samples were then sputter-coated with gold-
22 palladium for improved conductivity. Finally, the prepared samples were visualized using a JEOL
23 JSM6400 Scanning Electron Microscope at an accelerating voltage of 10 kV, enabling high-

1 resolution imaging of the yeast cells. To analyze the fractal dimension of SEM images of whole
2 cells and capsular-PS structures, we utilized the FracLac plugin of ImageJ
3 (<http://rsb.info.nih.gov/ij/plugins/fraclac/FLHelp/Introduction.htm>). The FracLac algorithm
4 quantifies the complexity of patterns in digital images, providing fractal dimensions data. The
5 algorithm works by scanning the input micrographs using a shifting grid algorithm, which allows
6 multiple scans from different locations on each image.

7

8

9 **RESULTS AND DISCUSSION**

10 **SANS Analysis of Exo-PS Solutions.** Based solely on the water-free composition, the neutron
11 scattering length density (SLD) of polysaccharides in H₂O is expected to range from $1 \times 10^{-6} \text{ \AA}^{-2}$ to
12 $2 \times 10^{-6} \text{ \AA}^{-2}$ (the SLD of pure H₂O is $-0.56 \times 10^{-6} \text{ \AA}^{-2}$)³³. The flat scattering profiles observed in the
13 exo-PS samples measured in H₂O are consistent with their high hydration state and a significant
14 contribution of incoherent scattering originating from the hydrogen atoms within the samples
15 (**Figure S2**). In the case of exo-PS solutions in D₂O, there is still a relatively strong incoherent
16 neutron scattering background observed in the reduced SANS data due to the non-labile hydrogen
17 atoms (**Figure 3**). The predominant M2 motif expected in our sample consists of three mannoses,
18 two xyloses, and one glucuronic acid²⁰, containing a significant number of labile hydrogens that
19 can exchange against D₂O during dialysis. However, non-labile and solvent-inaccessible hydrogen
20 atoms that remain at varying concentrations are responsible for the differences in background
21 intensities observed at high q in the SANS data for samples at 1 mg/mL, 5 mg/mL, and 10 mg/mL
22 exo-PS (**Figure 3**).

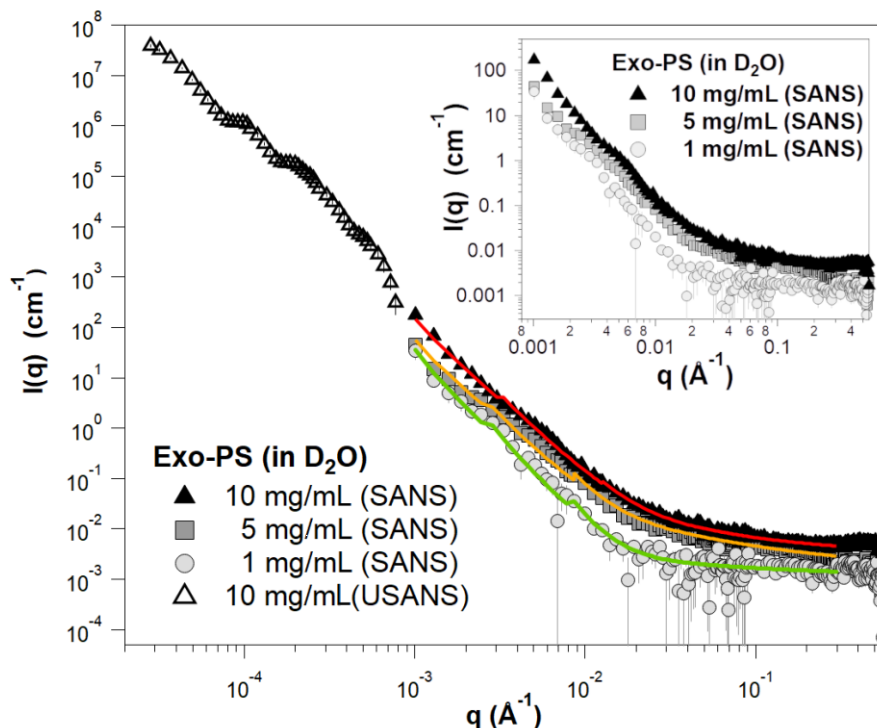
1 At low q values, the SANS data for the 10 mg/mL exo-PS in D₂O extend down to 0.001 Å⁻¹ and
2 exhibit a q -dependent intensity profile that reasonably matches the USANS data profile. This
3 indicates the reliability of the desmearing process (a correction applied to the experimental data to
4 account for the slit-smearing effects of the Bonse-Hart USANS instrument) and underscores the
5 consistency between the data collected for the sample in the two scattering regimes³⁴.

6 For q values below 0.003 Å⁻¹, the SANS scattered intensities of the exo-PS samples at 5 mg/mL
7 and 10 mg/mL display a very similar q^{-n} dependency characteristic of mass fractals (refer to the
8 Porod exponents in **Table S1**), with $n \approx 2.9$ reflecting a compact gel structure. An increase in inter-
9 cluster interactions is observed for the 5 mg/mL and 10 mg/mL exo-PS solutions, as indicated by
10 the larger Porod scales compared to those at 1 mg/mL exo-PS.

11 The fitting of the exo-PS SANS data produced a consistent correlation length for all
12 concentrations measured (48.9 ± 7.8 Å for 1 mg/mL exo-PS), which is approximately equivalent
13 to the length of four M2 triads (**Figure 4C**). The gelation of exo-PS contributes to the viscosity of
14 the solutions and yields a relatively small correlation length³⁵. While the presence of negatively
15 charged glucuronic acid (GlcA) residues can lead to chain-swelling due to electrostatic repulsion,
16 the occurrence of other interactions can stabilize polymer collapse and interchain
17 interactions^{23,36,37}. Namely, hydrogen bonds, van der Waals interactions, and ionic bridging which
18 can be promoted by the presence of the divalent cations Mg²⁺ and Ca²⁺ in the culture media²⁴. The
19 impact of ionic bridging in polysaccharide structure can be observed by the change in the SAXS
20 profile of exo-PS H₂O solutions treated with a chelating agent (see Figure S3).

21 For the 1 mg/mL exo-PS solution, below the overlap concentration, the fit to the SANS data
22 generated a Porod exponent of 3.28 ± 0.16 , consistent with a roughness or irregularity of the pores

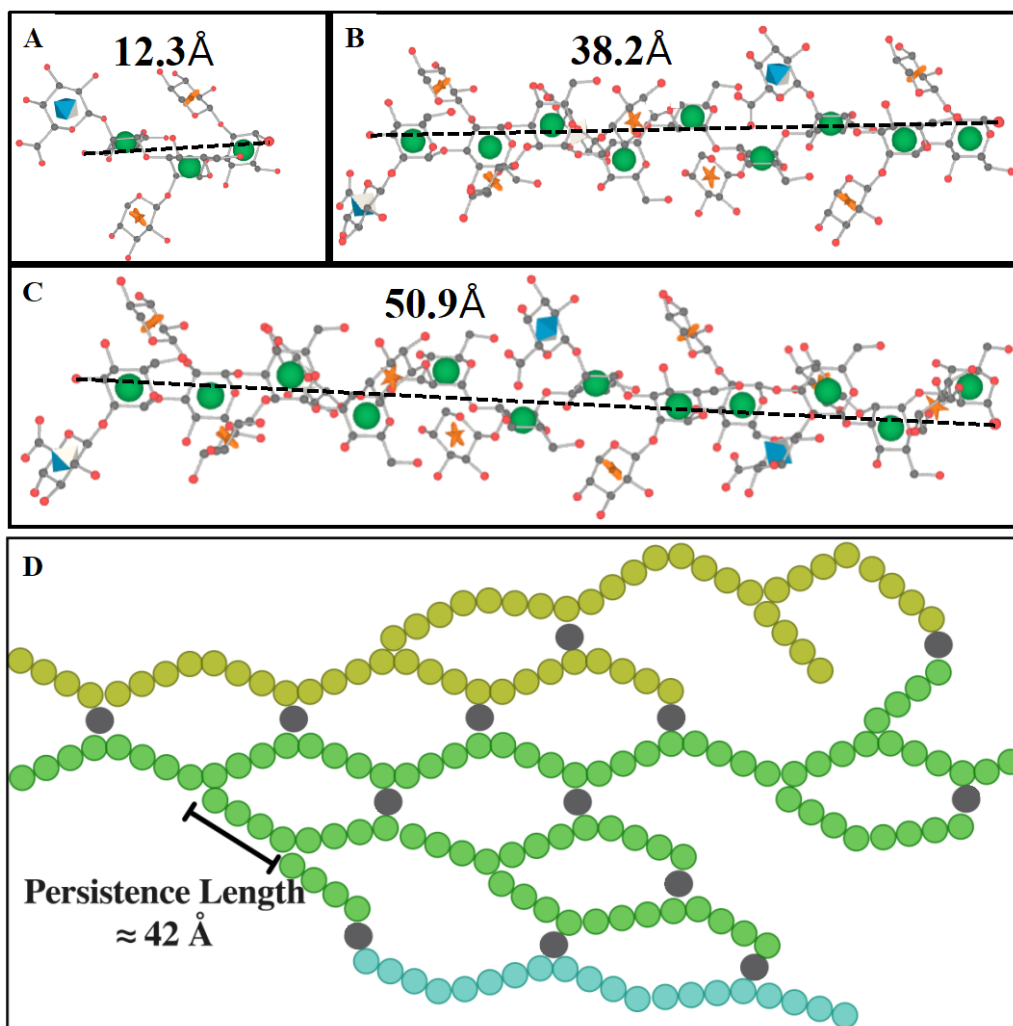
- 1 within the gel network, as illustrated by the schematic drawing in Figure 4D and supported by the
- 2 SEM data at a similar length scale.



3
4 **Figure 3.** Background-subtracted, reduced SANS, and USANS data for the exo-PS solutions in
5 D₂O at varying concentrations. The USANS data shown has been desmeared using the macro-
6 routines for Igor provided by the NCNR to account for the slit-smearing effects of the BT5
7 instrument on the experimental data. The solid lines depict SANS data fits for the solutions at 1
8 mg/mL (green), 5 mg/mL (orange), and 10 mg/mL (red) exo-PS; it should be noted that the small
9 discontinuities in the line fit at $q \approx 0.03 \text{ \AA}^{-1}$ and $q \approx 0.09 \text{ \AA}^{-1}$ are a resolution artifact related to the
10 instrumental configurations used for data collection and are not indicative of a sample-related
11 scattering characteristic. The inset provides an enlarged view of the SANS data to highlight the
12 distinctions observed between different concentrations. The error bars represent standard errors
13 derived from counting statistics and, when not visibly discernible, are smaller than the
14 corresponding data markers.

15
16 For the 5 mg/mL and 10 mg/mL exo-PS solutions, a discernable change in the q^{-n} dependency
17 of the SANS scattering intensities is observed at q values around 0.006 \AA^{-1} and beyond, where n
18 increases in its value (**Figure 3** inset). In the case of the 1 mg/mL exo-PS solution, however, due
19 to the poorer signal-to-noise ratio, such a transition is not as precisely defined.

1



2
3 **Figure 4.** Schematic representation of M2 motif and exo-PS in water for one M2 (A), three M2
4 (B), and four M2 (C) triads, drawn and energy minimized using GLYCAM³⁸. Residues are
5 represented by their symbol nomenclature: green sphere for mannose, orange star for xylose, and
6 blue diamond for GlcA. The distance between the two furthest oxygens that connect mannoses
7 was measured to determine the approximate length of one (12.3 Å), three (38.2 Å), or four (50.9 Å)
8 triads, respectively. (D) The exo-PS in water is drawn in 2D to suggest a compatible arrangement
9 of the exo-PS structure, where each circle (except gray circles that represent divalent cations)
10 represents one triad, and three exemplar chains are represented with different colors. A potential
11 pattern of intra- and inter-chain ionic bridging by the divalent cations such as Mg²⁺ and Ca²⁺
12 (represented by gray circles) present in the cell culture media. The corresponding estimated
13 persistence length (length of the region with rigid rod behavior) is approximately 42 Å. Image
14 created with BioRender.com.

15

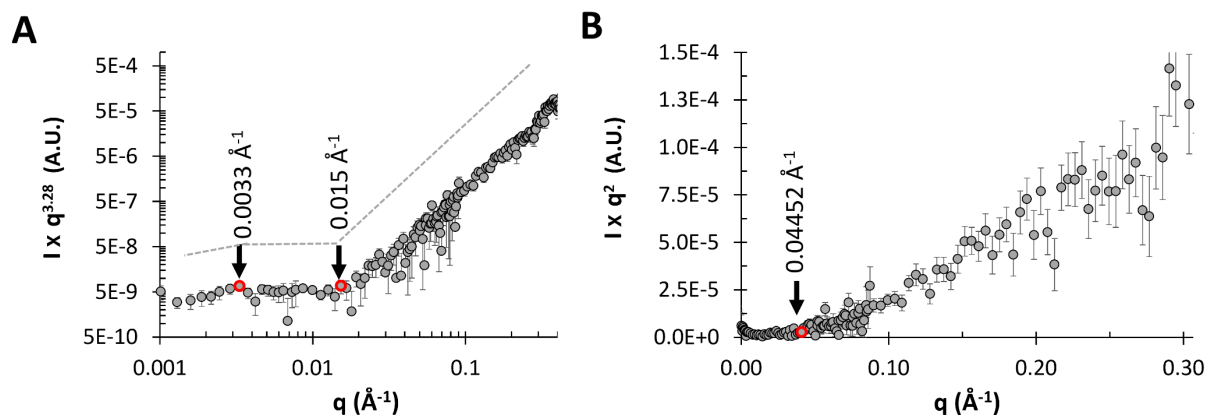


Figure 5. SANS data for 1 mg/mL exo-PS solution in D₂O, are shown as (A) Porod exponent-weighted intensities and (B) a standard Kratky plot.

The q -dependency of the SANS intensity was analyzed at various length scales for the 1 mg/mL exo-PS solution in Figure 5. The Porod region (Figure 5A) covers a q -range of approximately 0.003-0.015 \AA^{-1} , corresponding to structural dimensions within the range of $(2\pi/q) \approx 420$ -2090 \AA . This is followed by the Lorentz region, characterized by a q -dependency of q^{-1} . The standard Kratky plot (Figure 5B) shows that at higher q ranges, the profile shifts at $q^* \approx 0.045 \text{\AA}^{-1}$, indicating a rigid rod behavior on a local scale. At this length scale, the PS chain is expected to exhibit rigid rod-like behavior without reorientation or branching^{39,40}. The persistence length l can be calculated for an ideal Gaussian chain using the formula:

$$l = \frac{D}{q^*} \quad (3)$$

where D is a constant with a value of $6/\pi \approx 1.91$ ⁴⁰. Applying this approximation to the exo-PS polymer in this local regime, the estimated persistence length is $\approx 42 \text{\AA}$. This length is consistent with that of three or four M2 units, suggesting a rigid rod-like behavior with no interruption between triads within each block.

1 **Optical Microscopy, SANS, and USANS Analysis of Whole Fungal Cells.** Figure 6 and **Table**
2 **S2** present microscopy of *C. neoformans* H99 cells in different solutions. The microscopic images
3 reveal a relatively high degree of variation in terms of both cell size and capsule thickness for the
4 whole cell and gamma-irradiated cell suspensions. Without gamma irradiation, the average cell
5 diameter was $13.9 \pm 2.9 \mu\text{m}$ in D₂O and $13.2 \pm 3.3 \mu\text{m}$ in H₂O, while cells subjected to gamma
6 irradiation had an average cell diameter of $6.4 \pm 2.7 \mu\text{m}$ in D₂O and $7.2 \pm 2.9 \mu\text{m}$ in H₂O. The
7 average capsule thickness before gamma-irradiation was also measured: $4.0 \pm 1.4 \mu\text{m}$ in D₂O and
8 $3.6 \pm 1.5 \mu\text{m}$ in H₂O. Based on the microscopy data, the choice of solvents did not significantly
9 affect cell diameter or capsule thickness (unpaired t-test, $P > 0.05$, ns). However, gamma
10 irradiation removed most of the capsular-PS (unpaired t-test, $P < 0.0001$, ****).

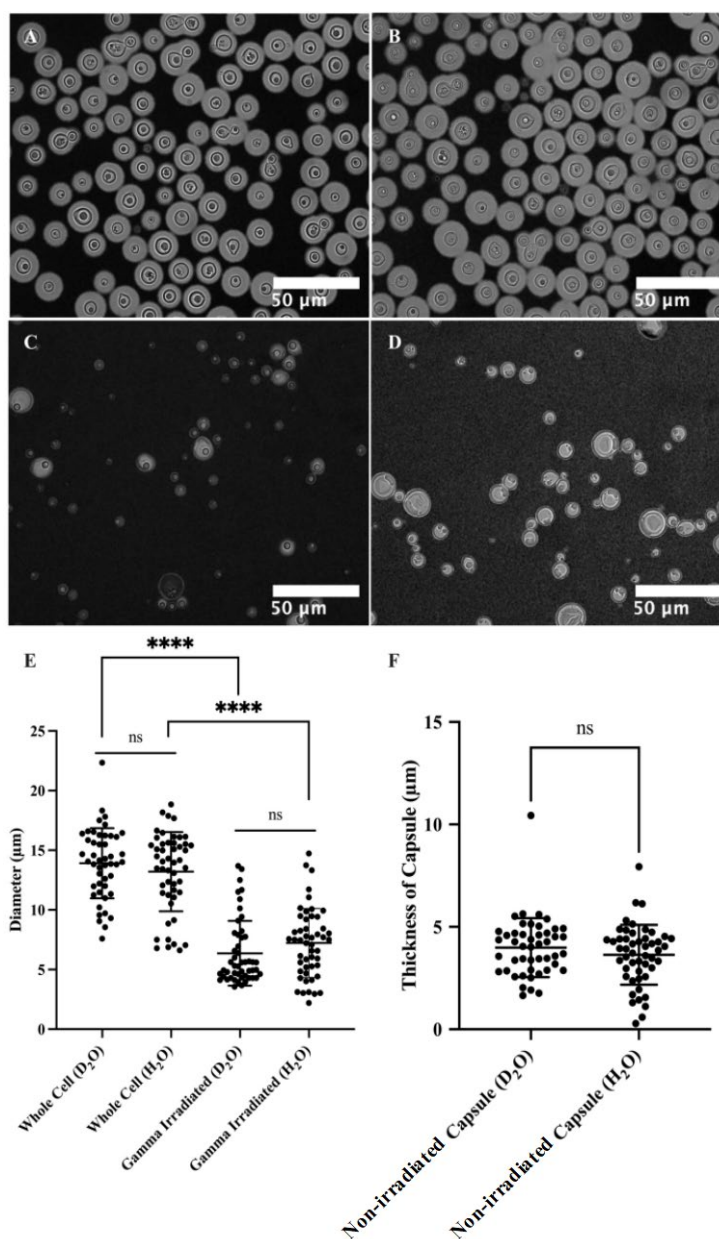
11 SANS and USANS data on whole and irradiated cells are presented in **Figure 7**, showing good
12 agreement between the desmeared USANS data and the SANS data. In H₂O, the scattering
13 intensities gradually decay with increasing q both for irradiated and whole cell samples, reaching
14 similar incoherent scattering background intensities of approximately $0.07 \text{ \AA}^{-1} - 0.08 \text{ \AA}^{-1}$,
15 dominated by contributions to incoherent scattering from the hydrogen atoms present. In contrast,
16 D₂O samples exhibit a substantially lower incoherent neutron scattering background, allowing a
17 discernable difference in the SANS profiles to emerge at $q > 0.1 \text{ \AA}^{-1}$. This range corresponds to
18 the expected contribution of the M2 triads towards scattering. Notably, at these higher q values,
19 gamma-irradiated samples display a distinct profile with a decrease in scattering intensities. This
20 observation is consistent with the disruption of the M2 triads that SANS detects for whole cells in
21 D₂O, but not in H₂O where it was observed that the Exo-PS scattering length density is matched
22 out. Differences are also evident in the Kratky plots for samples measured in D₂O, as present in
23 Figure S5 in the supporting information.

1 Given the high polydispersity of the samples, USANS data fitting was not attempted, as neutron
2 scattering probes a significant amount of bulk sample compared to the images in **Figure 6**.
3 Additionally, unknown contributions to the scattering profile from cellular components such as the
4 nucleus or the cell wall further complicate data fitting. The difference in size between whole and
5 gamma-irradiated cells is apparent from the USANS profiles for both H₂O and D₂O samples,
6 where the scattering profiles show a maximum intensity plateau at $tq < 0.00005 \text{ \AA}^{-1}$, as the
7 intensities reach the Guinier regime. The calculated radii of gyration for irradiated cell samples,
8 derived from Guinier analysis (**Figure S4** and **Table S3**), are consistent with the dimensions
9 observed by optical microscopy. For non-irradiated samples, insufficient data points were
10 collected in the Guinier regime, preventing an unambiguous calculation of the corresponding
11 larger cell radii of gyration.

12 Since exo-PS in H₂O solutions did not exhibit measurable contrast in the SANS regime, even at
13 concentrations of 10 mg/mL, the discernible discrepancies in cell size between whole and gamma-
14 irradiated cells in H₂O indicate differentiation between the exo-PS and capsular-PS. This is
15 consistent with a gradient of PS densities in the pristine whole cells, ranging from an outer, more
16 hydrated layer to an inner, denser layer closer to the cell wall, which is less solvent accessible and
17 more resistant to ablation²³.

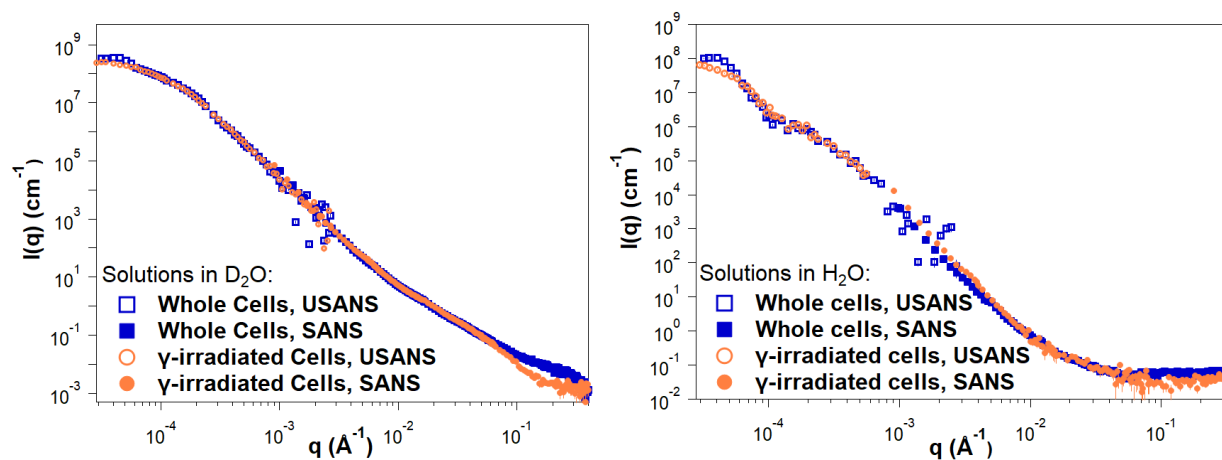
18 In the USANS data for H₂O solutions, there is an inflection point at $q \approx 0.0001 \text{ \AA}^{-1}$ that is absent
19 in the samples containing D₂O. Considering that no significant increase in polydispersity was
20 detected by optical microscopy for the samples in D₂O compared to H₂O, the absence of inflection
21 in D₂O solutions is not consistent with a resolution effect. Instead, the data may reflect a structural
22 characteristic of the fungal cell body for which the solutions in H₂O provide better SLD contrast.

- 1 Given the complexity of the fungal cell and the unknown SLD of the different cell components,
- 2 no specific structure or organelle can be objectively assigned to this area of the USANS profile.



3
4 **Figure 6.** Microscopy of *C. neoformans* H99 cells in water and the effect of gamma irradiation on
5 cellular and capsular dimensions. Samples were counterstained with India Ink particles, which are
6 excluded by the dense PS capsule. Cells without gamma irradiation were resuspended in D₂O (A)
7 and H₂O (B), and cells treated with 40 minutes of gamma irradiation were resuspended in D₂O (C)
8 and H₂O (D) as well. The cell diameters of all four samples were estimated (E), and capsule
9 thickness for whole cells was obtained as the differences between the radii of cells and cell bodies
10 (F). The t-test analyses are labeled based on their p-value (p > 0.05: ns; p < 0.05: *; p < 0.01: **;
11 p < 0.001: ***; p < 0.0001: ****).

1



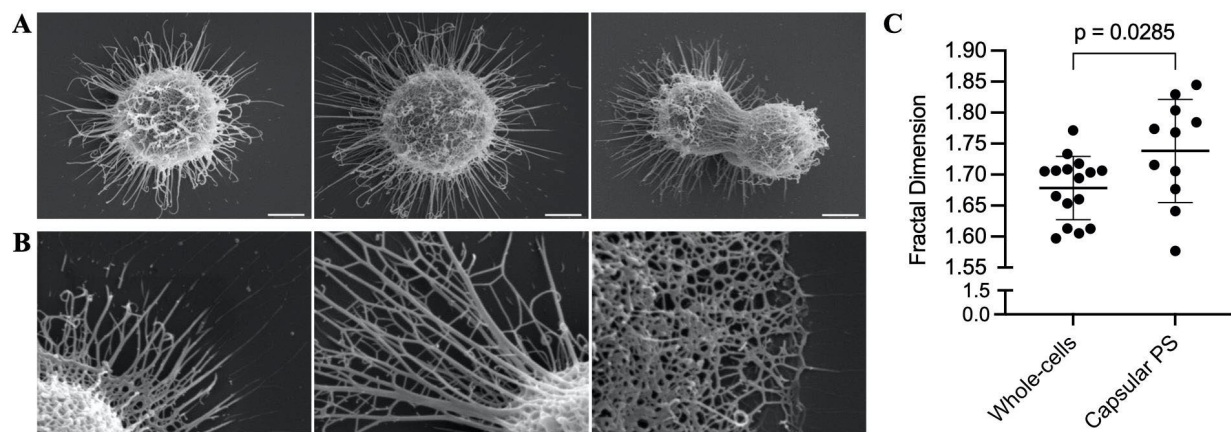
2

3 **Figure 7.** Reduced SANS (buffer subtracted) and USANS data collected for fungal cells in D₂O
4 and H₂O solutions, for both intact and gamma-irradiated cells. The desmeared USANS data
5 displayed compensates for the slit-smearing effects on the experimental data, allowing direct
6 comparison with the SANS data for each sample. Error bars represent standard errors from
7 counting statistics and are smaller than the corresponding data marker when not visible.

8

9 **Fractal Analysis of Scanning Electron Micrographs.** Image analysis of encapsulated whole
10 cells and capsular structures reveals fractal patterns with dimensions ranging from 1.6 to 1.85
11 (**Figure 8**). Despite these samples undergoing dehydration during SEM processing and thus not
12 being in their native state, the presence of fractal patterns in the polysaccharides is consistent with
13 the neutron scattering data in solution. Moreover, this fractal pattern was observed even after
14 capsule dehydration and the coalescing of PS molecules into thick fibrils. This suggests a
15 connection between the hydrated and dehydrated structures of polysaccharides, possibly reflecting
16 the fungus's resistance to dehydrating conditions.

17



1
2 **Figure 8.** Fractal analysis of SEM micrographs of whole encapsulated cells and capsular-PS
3 structures. (A) Representative whole encapsulated *C. neoformans* cells and (B) capsular-PS
4 structures, showing the fractal structure and the presence of an irregular pore network. Scale bars
5 represent 2 and 1 micrometers, respectively. (C) Fractal dimensions of 27 micrographs were
6 analyzed using the FracLac plugin in ImageJ.

10 CONCLUSIONS

11 This study demonstrates the effective use of neutron scattering and different neutron scattering
12 contrasts (utilizing solutions with 0% and 100% D₂O) to gain insights into the structural
13 characteristics of both *C. neoformans* exo-PS and cells under their native conditions. Our findings
14 present compelling evidence that exo-PS inherently exhibits mass fractal characteristics,
15 representing a self-similar branched system or network spanning a wide range of size scales. While
16 the presence of fractals in certain polysaccharides is not uncommon, the specific characteristics of
17 these fractals, such as fractal dimension, can vary widely due to multiple factors, such as molecular
18 composition, surrounding environment, and processing conditions^{6,22}.

19 The SANS results from exo-PS scattering are consistent with a collapsed chain-like behavior
20 stabilized by interchain and intrachain interactions, including divalent cation bridges between
21 negatively charged glucuronic acid residues, a phenomenon previously reported in the presence of

1 water molecules²⁵. Future SANS and USANS studies should address the concentration effects of
2 exo-PS on hydrogen-to-deuterium exchange levels and buffer accessibility (including chelating
3 agents if used to further investigate the role of cation bridging in the structuring of the
4 polysaccharide). High concentrations are likely to impact solvent buffer accessibility to the
5 polysaccharide, while lower concentrations may favor more uniformly chain-hydrated states and
6 minimize scattering effects arising from overlapping and entanglement.

7 The observed rigid rod behavior of exo-PS at local scales, with an estimated persistence length
8 of approximately 42 Å, suggests that the arrangement of three to four GXM triads, particularly the
9 M2 motif, involves short repeats where the chain direction may change at the end of each repeat,
10 resulting in an overall semi-flexible structure. This local-scale rigidity of exo-PS agrees with
11 molecular modeling studies, which propose that, at least within six GXM motifs, the ends of the
12 chain do not bend into close proximity⁴¹.

13 As a dominant virulence factor often targeted for antibody treatment, exo-PS plays a crucial role
14 in infection. Recent research has identified deca-saccharide (serotype A) as a possible minimal size
15 for effective neutralizing mAb recognition, but our data offer a broader range of oligosaccharide
16 sizes suitable for testing immune responses⁴². To better characterize the exo-PS secreted in humans
17 during infection, similar studies on exo-PS secreted by isolated infecting fungal cells cultured in
18 media with the cation compositions of human fluids should be conducted to explore the effects of
19 different types and concentrations of counterions.

20 It is important to note that sample preparation protocols can influence the measured structural
21 properties, as previously suggested¹⁰. It cannot be overstated that the experimental data reflects
22 only the structural features of the selected sample. Varying molar mass cutoffs during filtration
23 can result in significant differences in the USANS regime (data not shown) and previous studies

1 have shown that *C. neoformans* GXM fractions of different molar masses are functionally
2 distinct⁴³. Further work is needed to systematically characterize USANS and microscopy data for
3 exo-PS chains representing the range of molar masses found *in vivo*.

4 Lastly, future SANS studies could utilize isotope-labeled dextrose or specific precursors to
5 enhance the contributions of capsular-PS to the overall scattering profiles measured from whole
6 cells, with the goal of further elucidating the differences between capsular-PS and exo-PS¹⁰.

7

8

9 **ASSOCIATED CONTENT**

10 **Supporting Information:** dynamic light scattering analysis of exo-PS, neutron, and X-ray
11 scattering data and data fitting for exo-PS samples, microscopy data for whole cell samples, and
12 Guinier fittings and Kratky plots for the fungal cell samples based on USANS and SANS data,
13 respectively (PDF).

14

15 **AUTHOR INFORMATION**

16 **Corresponding Authors**

17 *E-mail: susanat@udel.edu.

18 *E-mail: rcorder4@jhu.edu.

19 **Author Contributions**

20 RJBC and SCMT designed the neutron scattering experimental approach. CS and RJBC designed
21 the cell culture and polysaccharide isolation protocols, prepared samples, and collected optical
22 microscopy data. SCMT and CS collected and reduced the neutron scattering data. SCMT and ZW

1 carried out the data fitting and analyses. AB carried out the fractal dimension analysis on SEM
2 images. The manuscript was written through the contributions of all authors. All authors have
3 approved the final version of the manuscript.

Notes

The authors declare no competing financial interest.

ACKNOWLEDGMENT

This work benefited from the use of the SasView application, originally developed under NSF award DMR-0520547. SasView contains code developed with funding from the European Union's Horizon 2020 research and innovation program under the SINE2020 project, grant agreement No 654000. SCMT is grateful for funding from the cooperative agreement #70NANB20H133 from NIST, U.S. Department of Commerce. We acknowledge the support of the National Institute of Standards and Technology, U.S. Department of Commerce, in providing the neutron research facilities used in this work. This work utilized facilities supported in part by the National Science Foundation under Agreement No. DMR-0944772. Certain commercial equipment, software, instruments, and materials are identified to foster understanding. Such identification does not imply recommendation or endorsement by the National Institute of Standards and Technology, nor does it imply that the materials or equipment identified are necessarily the best available for the purpose. The statements, findings, conclusions, and recommendations are those of the authors and do not necessarily reflect the view of NIST or the U.S. Department of Commerce. RJBC was supported by the Johns Hopkins University Center for AIDS Research (P30AI094189). The authors also thank Dr. Scott A. McConnell for reviewing the data and providing valuable input.

ABBREVIATIONS

PS, polysaccharide; GXM, Glucuronoxylomannans; SANS, small-angle neutron scattering; USANS, ultra-small-angle neutron scattering; SEM, scanning electron microscopy; SLD, scattering length density.

REFERENCES

- (1) Rajasingham, R.; Smith, R. M.; Park, B. J.; Jarvis, J. N.; Govender, N. P.; Chiller, T. M.; Denning, D. W.; Loyse, A.; Boulware, D. R. Global Burden of Disease of HIV-Associated Cryptococcal Meningitis: An Updated Analysis. *Lancet Infect. Dis.* **2017**, *17* (8), 873–881. [https://doi.org/10.1016/s1473-3099\(17\)30243-8](https://doi.org/10.1016/s1473-3099(17)30243-8).
- (2) Ngan, N. T. T.; Flower, B.; Day, J. N. Treatment of Cryptococcal Meningitis: How Have We Got Here and Where Are We Going? *Drugs* **2022**, *82* (12), 1237–1249. <https://doi.org/10.1007/s40265-022-01757-5>.
- (3) Pappas, P. G.; Perfect, J. R.; Cloud, G. A.; Larsen, R. A.; Pankey, G. A.; Lancaster, D. J.; Henderson, H.; Kauffman, C. A.; Haas, D. W.; Saccente, M.; Hamill, R. J.; Holloway, M. S.; Warren, R. M.; Dismukes, W. E. Cryptococcosis in Human Immunodeficiency Virus-Negative Patients in the Era of Effective Azole Therapy. *Clin. Infect. Dis.* **2001**, *33* (5), 690–699. <https://doi.org/10.1086/322597>.
- (4) Casadevall, A.; Coelho, C.; Cordero, R. J. B.; Dragotakes, Q.; Jung, E.; Vij, R.; Wear, M. P. The Capsule of *Cryptococcus Neoformans*. *Virulence* **2019**, *10* (1), 822–831. <https://doi.org/10.1080/21505594.2018.1431087>.

(5) Maxson, M. E.; Cook, E.; Casadevall, A.; Zaragoza, O. The Volume and Hydration of the *Cryptococcus Neoformans* Polysaccharide Capsule. *Fungal Genet. Biol.* **2007**, *44* (3), 180–186. <https://doi.org/10.1016/j.fgb.2006.07.010>.

(6) Wear, M. P.; Hargett, A. A.; Kelly, J. E.; McConnell, S. A.; Crawford, C. J.; Freedberg, D. I.; Stark, R. E.; Casadevall, A. Lyophilization Induces Physicochemical Alterations in Cryptococcal Exopolysaccharide. *Carbohydr. Polym.* **2022**, *291*, 119547. <https://doi.org/10.1016/j.carbpol.2022.119547>.

(7) Cordero, R. J. B.; Pontes, B.; Frases, S.; Nakouzi, A. S.; Nimrichter, L.; Rodrigues, M. L.; Viana, N. B.; Casadevall, A. Antibody Binding to *Cryptococcus Neoformans* Impairs Budding by Altering Capsular Mechanical Properties. *J. Immunol.* **2013**, *190* (1), 317–323. <https://doi.org/10.4049/jimmunol.1202324>.

(8) Bowen, A.; Wear, M. P.; Cordero, R. J. B.; Oscarson, S.; Casadevall, A. A Monoclonal Antibody to *Cryptococcus Neoformans* Glucuronoxylomannan Manifests Hydrolytic Activity for Both Peptides and Polysaccharides*. *J. Biol. Chem.* **2017**, *292* (2), 417–434. <https://doi.org/10.1074/jbc.m116.767582>.

(9) Cordero, R. J. B.; Pontes, B.; Guimarães, A. J.; Martinez, L. R.; Rivera, J.; Fries, B. C.; Nimrichter, L.; Rodrigues, M. L.; Viana, N. B.; Casadevall, A. Chronological Aging Is Associated with Biophysical and Chemical Changes in the Capsule of *Cryptococcus Neoformans*. *Infect. Immun.* **2011**, *79* (12), 4990–5000. <https://doi.org/10.1128/iai.05789-11>.

(10) Frases, S.; Nimrichter, L.; Viana, N. B.; Nakouzi, A.; Casadevall, A. *Cryptococcus Neoformans* Capsular Polysaccharide and Exopolysaccharide Fractions Manifest Physical,

Chemical, and Antigenic Differences. *Eukaryot. cell* **2007**, *7* (2), 319–327.
<https://doi.org/10.1128/ec.00378-07>.

(11) Frases, S.; Pontes, B.; Nimrichter, L.; Rodrigues, M. L.; Viana, N. B.; Casadevall, A. The Elastic Properties of the *Cryptococcus Neoformans* Capsule. *Biophys. J.* **2009**, *97* (4), 937–945.
<https://doi.org/10.1016/j.bpj.2009.04.043>.

(12) Fonseca, F. L.; Nohara, L. L.; Cordero, R. J. B.; Frases, S.; Casadevall, A.; Almeida, I. C.; Nimrichter, L.; Rodrigues, M. L. Immunomodulatory Effects of Serotype B Glucuronoxylomannan from *Cryptococcus Gattii* Correlate with Polysaccharide Diameter. *Infect. Immun.* **2010**, *78* (9), 3861–3870. <https://doi.org/10.1128/iai.00111-10>.

(13) Cordero, R. J. B.; Frases, S.; Guimarães, A. J.; Rivera, J.; Casadevall, A. Evidence for Branching in Cryptococcal Capsular Polysaccharides and Consequences on Its Biological Activity. *Mol. Microbiol.* **2011**, *79* (4), 1101–1117. <https://doi.org/10.1111/j.1365-2958.2010.07511.x>.

(14) Ellerbroek, P. M.; Lefeber, D. J.; Veghel, R. van; Scharringa, J.; Brouwer, E.; Gerwig, G. J.; Janbon, G.; Hoepelman, A. I. M.; Coenjaerts, F. E. J. O-Acetylation of Cryptococcal Capsular Glucuronoxylomannan Is Essential for Interference with Neutrophil Migration. *J. Immunol.* **2004**, *173* (12), 7513–7520. <https://doi.org/10.4049/jimmunol.173.12.7513>.

(15) Belay, T.; Cherniak, R.; Kozel, T. R.; Casadevall, A. Reactivity Patterns and Epitope Specificities of Anti-*Cryptococcus Neoformans* Monoclonal Antibodies by Enzyme-Linked Immunosorbent Assay and Dot Enzyme Assay. *Infect. Immun.* **1997**, *65* (2), 718–728.
<https://doi.org/10.1128/iai.65.2.718-728.1997>.

(16) Frases, S.; Pontes, B.; Nimrichter, L.; Viana, N. B.; Rodrigues, M. L.; Casadevall, A. Capsule of *Cryptococcus Neoformans* Grows by Enlargement of Polysaccharide Molecules. *Proc. Natl. Acad. Sci.* **2009**, *106* (4), 1228–1233. <https://doi.org/10.1073/pnas.0808995106>.

(17) McFadden, D. C.; Fries, B. C.; Wang, F.; Casadevall, A. Capsule Structural Heterogeneity and Antigenic Variation in *Cryptococcus Neoformans*. *Eukaryot. Cell* **2007**, *6* (8), 1464–1473. <https://doi.org/10.1128/ec.00162-07>.

(18) Casadevall, A.; Nakouzi, A.; Crippa, P. R.; Eisner, M. Fungal Melanins Differ in Planar Stacking Distances. *PLoS ONE* **2012**, *7* (2), e30299. <https://doi.org/10.1371/journal.pone.0030299>.

(19) Cherniak, R.; Valafar, H.; Morris, L. C.; Valafar, F. *Cryptococcus Neoformans* Chemotyping by Quantitative Analysis of ¹H Nuclear Magnetic Resonance Spectra of Glucuronoxylomannans with a Computer-Simulated Artificial Neural Network. *Clin. Diagn. Lab. Immunol.* **1998**, *5* (2), 146–159. <https://doi.org/10.1128/cdli.5.2.146-159.1998>.

(20) Nakouzi, A.; Zhang, T.; Oscarson, S.; Casadevall, A. The Common *Cryptococcus Neoformans* Glucuronoxylomannan M2 Motif Elicits Non-Protective Antibodies. *Vaccine* **2009**, *27* (27), 3513–3518. <https://doi.org/10.1016/j.vaccine.2009.03.089>.

(21) Cheng, K.; Zhou, Y.; Neelamegham, S. Drawglycan-SNFG: A Robust Tool to Render Glycans and Glycopeptides with Fragmentation Information. *Glycobiology* **2017**, *27* (3), 200–205. <https://doi.org/10.1093/glycob/cww115>.

(22) Yu, L.; Yakubov, G. E.; Gilbert, E. P.; Sewell, K.; van de Meene, A. M. L.; Stokes, J. R. Multi-Scale Assembly of Hydrogels Formed by Highly Branched Arabinoxylans from *Plantago*

Ovata Seed Mucilage Studied by USANS/SANS and Rheology. *Carbohydr. Polym.* **2019**, *207*, 333–342. <https://doi.org/10.1016/j.carbpol.2018.11.098>.

(23) Maxson, M. E.; Dadachova, E.; Casadevall, A.; Zaragoza, O. Radial Mass Density, Charge, and Epitope Distribution in the *Cryptococcus Neoformans* Capsule. *Eukaryot. Cell* **2007**, *6* (1), 95–109. <https://doi.org/10.1128/ec.00306-06>.

(24) Bryan, R. A.; Zaragoza, O.; Zhang, T.; Ortiz, G.; Casadevall, A.; Dadachova, E. Radiological Studies Reveal Radial Differences in the Architecture of the Polysaccharide Capsule of *Cryptococcus Neoformans*. *Eukaryot. Cell* **2005**, *4* (2), 465–475. <https://doi.org/10.1128/ec.4.2.465-475.2005>.

(25) Nimrichter, L.; Frases, S.; Cinelli, L. P.; Viana, N. B.; Nakouzi, A.; Travassos, L. R.; Casadevall, A.; Rodrigues, M. L. Self-Aggregation of *Cryptococcus Neoformans* Capsular Glucuronoxylomannan Is Dependent on Divalent Cations. *Eukaryot. cell* **2007**, *6* (8), 1400–1410. <https://doi.org/10.1128/ec.00122-07>.

(26) Masuko, T.; Minami, A.; Iwasaki, N.; Majima, T.; Nishimura, S.-I.; Lee, Y. C. Carbohydrate Analysis by a Phenol–Sulfuric Acid Method in Microplate Format. *Anal. Biochem.* **2005**, *339* (1), 69–72. <https://doi.org/10.1016/j.ab.2004.12.001>.

(27) Vadhillo, D. C.; Mathues, W.; Clasen, C. Microsecond Relaxation Processes in Shear and Extensional Flows of Weakly Elastic Polymer Solutions. *Rheol. Acta* **2012**, *51* (8), 755–769. <https://doi.org/10.1007/s00397-012-0640-z>.

(28) Ying, Q.; Chu, B. Overlap Concentration of Macromolecules in Solution. *Macromolecules* **1987**, *20* (2), 362–366. <https://doi.org/10.1021/ma00168a023>.

(29) Glinka, C. J.; Barker, J. G.; Hammouda, B.; Krueger, S.; Moyer, J. J.; Orts, W. J. The 30 m Small-Angle Neutron Scattering Instruments at the National Institute of Standards and Technology. *J. Appl. Crystallogr.* **1998**, *31* (3), 430–445. <https://doi.org/10.1107/s0021889897017020>.

(30) Barker, J. G.; Glinka, C. J.; Moyer, J. J.; Kim, M. H.; Drews, A. R.; Agamalian, M. Design and Performance of a Thermal-Neutron Double-Crystal Diffractometer for USANS at NIST. *J. Appl. Crystallogr.* **2005**, *38* (6), 1004–1011. <https://doi.org/10.1107/s0021889805032103>.

(31) Kline, S. R. Reduction and Analysis of SANS and USANS Data Using IGOR Pro. *J. Appl. Crystallogr.* **2006**, *39* (6), 895–900. <https://doi.org/10.1107/s0021889806035059>.

(32) Hammouda, B.; Ho, D. L.; Kline, S. Insight into Clustering in Poly(Ethylene Oxide) Solutions. *Macromolecules* **2004**, *37* (18), 6932–6937. <https://doi.org/10.1021/ma049623d>.

(33) Gilbert, E. P. Small-angle X-ray and Neutron Scattering in Food Colloids. *Curr. Opin. Colloid Interface Sci.* **2019**, *42*, 55–72. <https://doi.org/10.1016/j.cocis.2019.03.005>.

(34) Jaksch, S.; Pipich, V.; Frielinghaus, H. Multiple Scattering and Resolution Effects in Small-Angle Neutron Scattering Experiments Calculated and Corrected by the Software Package Muscatt. *J. Appl. Crystallogr.* **2021**, *54* (6), 1580–1593. <https://doi.org/10.1107/S1600576721009067>.

(35) Hyland, L. L.; Taraban, M. B.; Hammouda, B.; Yu, Y. B. Mutually Reinforced Multicomponent Polysaccharide Networks. *Biopolymers* **2011**, *95* (12), 840–851. <https://doi.org/10.1002/bip.21687>.

(36) Muller, F.; Manet, S.; Jean, B.; Chambat, G.; Boué, F.; Heux, L.; Cousin, F. SANS Measurements of Semiflexible Xyloglucan Polysaccharide Chains in Water Reveal Their Self-Avoiding Statistics. *Biomacromolecules* **2011**, *12* (9), 3330–3336. <https://doi.org/10.1021/bm200881x>.

(37) McFadden, D.; Zaragoza, O.; Casadevall, A. The Capsular Dynamics of *Cryptococcus Neoformans*. *Trends Microbiol.* **2006**, *14* (11), 497–505. <https://doi.org/10.1016/j.tim.2006.09.003>.

(38) *GLYCAM-Web | Utilities for molecular modeling of carbohydrates*. Woods Group. <http://glycam.org> (accessed 2023-11-01).

(39) Rosales, A. M.; Murnen, H. K.; Kline, S. R.; Zuckermann, R. N.; Segalman, R. A. Determination of the Persistence Length of Helical and Non-Helical Polypeptoids in Solution. *Soft Matter* **2012**, *8* (13), 3673–3680. <https://doi.org/10.1039/c2sm07092h>.

(40) Gupta, A. K.; Cotton, J. P.; Marchal, E.; Burchard, W.; Benoit, H. Persistence Length of Cellulose Tricarbanilate by Small-Angle Neutron Scattering. *Polymer* **1976**, *17* (5), 363–366. [https://doi.org/10.1016/0032-3861\(76\)90228-7](https://doi.org/10.1016/0032-3861(76)90228-7).

(41) Kuttel, M. M.; Casadevall, A.; Oscarson, S. *Cryptococcus Neoformans* Capsular GXM Conformation and Epitope Presentation: A Molecular Modelling Study. *Molecules* **2020**, *25* (11), 2651. <https://doi.org/10.3390/molecules25112651>.

(42) Guazzelli, L.; Crawford, C. J.; Ulc, R.; Bowen, A.; McCabe, O.; Jedlicka, A. J.; Wear, M. P.; Casadevall, A.; Oscarson, S. A Synthetic Glycan Array Containing *Cryptococcus Neoformans*

Glucuronoxylomannan Capsular Polysaccharide Fragments Allows the Mapping of Protective Epitopes. *Chem. Sci.* **2020**, *11* (34), 9209–9217. <https://doi.org/10.1039/d0sc01249a>.

(43) Albuquerque, P. C.; Fonseca, F. L.; Dutra, F. F.; Bozza, M. T.; Frases, S.; Casadevall, A.; Rodrigues, M. L. Cryptococcus Neoformans Glucuronoxylomannan Fractions of Different Molecular Masses Are Functionally Distinct. *Futur. Microbiol.* **2014**, *9* (2), 147–161. <https://doi.org/10.2217/fmb.13.163>.